

Ultrafast evanescent heat transfer across solid interfaces via hyperbolic phonon–polariton modes in hexagonal boron nitride

Received: 13 July 2023

Accepted: 27 January 2025

Published online: 17 March 2025

 Check for updates

William Hutchins¹, Saman Zare¹, Dan M. Hirt¹, John A. Tomko¹, Joseph R. Matson², Katja Diaz-Granados², Mackey Long III³, Mingze He³, Thomas Pfeifer¹, Jiahan Li⁴, James H. Edgar⁴, Jon-Paul Maria⁵, Joshua D. Caldwell^{2,3}✉ & Patrick E. Hopkins^{1,6,7}✉

Thermal transport across solid–solid interfaces is vital for advanced electronic and photonic applications, yet conventional conduction pathways often restrict performance. In polar crystals, hybridized vibrational modes called phonon polaritons offer a promising avenue to overcome the limitations of intrinsic phonon heat conduction. Here our work demonstrates that volume-confined hyperbolic phonon polariton (HPhP) modes can transfer energy across solid–solid interfaces at rates far exceeding phonon–phonon conduction. Using pump–probe thermorefectance with a mid-infrared, tunable probe pulse with subpicosecond resolution, we remotely and selectively observe HPhP modes in hexagonal boron nitride (hBN) via broadband radiative heating from a gold source. Our measurements ascertain that hot electrons impinging at the interface radiate directly into the HPhPs of hBN in the near field, bypassing the phonon–phonon transport pathway. Such polaritonic coupling enables thermal transport speeds in solids orders of magnitude faster than possible through diffusive phonon processes. We thereby showcase a pronounced thermal transport enhancement across the gold–hBN interface via phonon–polariton coupling, advancing the limits of interfacial heat transfer.

Across nearly all heterogeneous dielectric interfaces, heat is dissipated via conductive processes driven by acoustic phonons or other vibrational interactions, which limit thermal boundary conductance (TBC)^{1–3}. Bose–Einstein statistics of nearly thermalized phononic distributions dictate that the typical vibrational energies that contribute to heat transfer across and away from interfaces are lower-energy, higher group-velocity acoustic phonons, which, at room temperature, are on the order of a few to 10 THz. Owing to their larger heat capacities⁴,

optical phonon branches play an important role in mediating thermal transport⁵. However, the intrinsically slow group velocities⁵ restrict these modes' abilities to spread heat away from interfaces and hot spots, thereby putting the burden of thermal dissipation back on the acoustic modes.

In this study, we examine an alternative mechanism to transfer energy across and away from all-solid heterogeneous interfaces by harnessing the local evanescent fields resulting from a hot radiating

A full list of affiliations appears at the end of the paper. ✉e-mail: josh.caldwell@vanderbilt.edu; phopkins@virginia.edu

source to directly launch volume-confined, hyperbolic phonon polaritons (HPhPs) within the frequency range bound by the transverse (TO) and longitudinal (LO) optical phonons of a polar crystalline material, which is referred to as the Reststrahlen band⁷. Hyperbolic polaritons are supported within spectral ranges where a material or structure exhibits dielectric permittivity that are opposite in sign along different crystal axes⁸. Originally explored in metal/dielectric superlattices in the form of hyperbolic metamaterials, HPhPs have been of substantial research interest as they can be supported in a homogeneous, low-loss film, with hexagonal boron nitride (hBN) serving as an exemplary material in this regard^{9–11}. Isotopic enrichment can also be leveraged to tune the Reststrahlen band and increase the phonon lifetimes (and thus polariton propagation lengths) of hBN and therefore tune the efficiency of the coupling mechanism^{10,12,13}, which here was employed to provide optimal propagation lengths. More recently, it has been demonstrated that natural, low-symmetry (highly anisotropic) crystals, such as orthorhombic MoO₃ (refs. 14,15) and V₂O₅ (ref. 16) and monoclinic crystals, such as β -Ga₂O₃ (ref. 17) and CdWO₄ (ref. 18) can support HPhPs that can be restricted to propagate along a specific direction in space, with the latter two supporting so-called hyperbolic shear polaritons that are not only highly directional, but also exhibit a propagation direction that is frequency dependent. As such, if these modes can be induced to carry heat, similar studies could also be widely applied to other hyperbolic materials along specific crystallographic directions via optimal material selection. Specifically, MoO₃ (ref. 15) and twisted metastructures¹⁹ also support highly directional confined HPhP modes, and heating of such modes would allow for directional thermal mitigation of hot spots across interfaces.

While optical phonons typically cannot be used to efficiently conduct heat away from interfaces owing to their slow group velocities, this seemingly insurmountable intrinsic material limitation can be overcome by transducing the broadband radiative thermal energy from a thin metal film in the near field into the HPhPs supported within the underlying anisotropic medium, passing this energy across the heterogeneous interface. Previously, HPhPs in hBN have been demonstrated to have propagation lengths of several micrometres^{19,20}, enabling applications, such as hyperlensing^{21–23} and chemical sensing, to enhance thermal transport beyond phonon-limited processes²⁴, and a Reststrahlen band that can exhibit reasonable emission even at near room temperatures²⁵. Literature has even suggested that this process can occur at interfaces between two-dimensional (2D) van der Waal materials^{26–28}, warranting the study of this process at three-dimensional (3D) contacts, a direct experimental measurement of which would demonstrate the broad applicability of this unique heat transfer process. Through exploiting time-resolved infrared (IR) pump–probe measurements, we directly measure the picosecond cooling of indirectly heated optical modes^{29,30} in a nearly isotopically pure hBN (h¹¹BN; >99%) flake after the optical pumping of an adjacent gold contact, thereby demonstrating a mechanism for interfacial cooling that is orders of magnitude faster than typical phonon-mediated processes. Previous works have demonstrated fast, efficient near-field radiative heat transfer (NFRHT) across narrow vacuum gaps between metallic and dielectric plates²⁵, but this approach relies on the inclusion of a nanometre-scale vacuum gap, thus limiting its utility in certain practices. Our work proves that TBC across heterogeneous interfaces and thermal dissipation in a material away from interfaces can be significantly enhanced through the coupling of a broadband radiating hot spot into propagating PhPs, a finding that surpasses intrinsic material limitations of thermal coupling at interfaces. In doing so, we establish a new paradigm for interfacial thermal transport that moves beyond the nearly century-old concepts and theories of phonon coupling at dielectric interfaces originally discovered by Kapitza³¹.

Enhanced thermal dissipation in solids via polaritonic heat transfer has been theoretically predicted³², and the prospect of enhanced speeds and even directional control of heat transfer is enabled by the

exotic properties of PhPs, such as long propagation lengths^{19,20}, anisotropic and nonuniform control of their propagation^{17,33–35} and speeds that approach per cent levels of the speed of light^{36–39}. Experimental works have shown the ability of HPhPs to enhance thermal conductance in dielectrics^{24,40}, however, experimental evidence differentiating the coupled PhP modes from the thermalized phonon modes intrinsic to the material is still lacking. Thus, the first major finding of our work is the ability to both spectrally and temporally resolve the thermally excited HPhP modes in hBN, providing clear evidence of the more efficient thermal transport that these hot HPhP carriers can provide.

Second, our results illustrate that HPhP thermal coupling can occur across an all-solid heterogeneous interface, and further that the HPhP modes do not need to be coherently excited, but rather can be optically stimulated by a greybody radiating in the near field. The latter observation is consistent with ref. 41, where thermal radiation from a heated SiC diffraction grating resulted in the excitation of propagating SPhPs, which once stimulated were outcoupled via diffraction, giving rise to spatially coherent IR radiation. It is well known that polaritonic modes can enhance heat transfer via NFRHT processes between two radiating bodies separated by a vacuum gap that is less than the Wien wavelength^{42–47}. Our work unlocks the possibility of utilizing this NFRHT enhancement at solid–solid interfaces in intimate atomistic contact by showing that this broadband radiative cooling effect is driven by PhP coupling that can delocalize the thermal energy from a radiating spot into an adjacent hyperbolic medium. This finding will redefine cooling of hot spots in materials and systems limited or dictated by interfacial resistances, such as high power or high frequency electronics⁴⁸, photonic circuits⁴⁹, memory⁵⁰ and thermophotovoltaics⁵¹.

Pump–probe measurements

Our sample geometry is designed to provide a direct observation of spectrally dependent radiative thermal coupling from a thermally excited source (50-nm Au pad) into HPhPs supported in h¹¹BN, referred to hence forth as hBN (Fig. 1a). In our pump–probe experiments, we excite the Au pad (Fig. 1b) with a 520-nm pump pulse (incident fluence upward of 0.3 GW m^{−2}) and a 200 μ m 1/e² diameter probe pulse centred on the Au pad. The central Au pad acts as the focal point of our experiment. We first overlap our pump and probe on the Si substrate. Then, we alter the position of the sample such that the green pump is focused on the circular pad. The rectangular pads serve as reflectors for the polaritons. This configuration creates standing polaritons, similar to ref. 19, in the space spanned by the probing region, which should increase our pump–probe signal. The different distances were used to be agnostic to the mean free paths of different HPhP modes. The thermorefectance changes, measured by the reflected probe pulses from the hBN as a function of time after pump absorption by the Au, are monitored as a function of probe wavelength, which are tuned from below to above the Reststrahlen band of hBN ($-1,355$ – $1,610$ cm^{−1})¹². Immediately following the pump absorption on the surface of the Au, the Au pad is rapidly volumetrically thermalized via ballistic electron transport⁵², which despite the low thermal emissivity of metals within the mid-IR will radiate efficiently in the near field owing to the large imaginary contribution to the Au dielectric permittivity or optical loss. Such near-field radiation is composed of high-momentum evanescent fields that can directly match the momenta of the HPhPs within the hBN slab. This coupling mechanism is present through the entire area of the Au–hBN interface, a mechanism that our experiment is designed to detect with our tunable IR probe energies. The enhanced coupling between the optical modes and the radiation underneath the pad give rise to large thermorefectance optical signals within the Reststrahlen band and at the TO phonon frequency of hBN, as shown in the contour plots of the thermorefectance spectra versus pump–probe delay time in Fig. 1c. In contrast, in the absence of the Au pad, we do not observe any such increase in thermorefectance signal as the hBN is transparent to the pump wavelength. This large spectral dependence

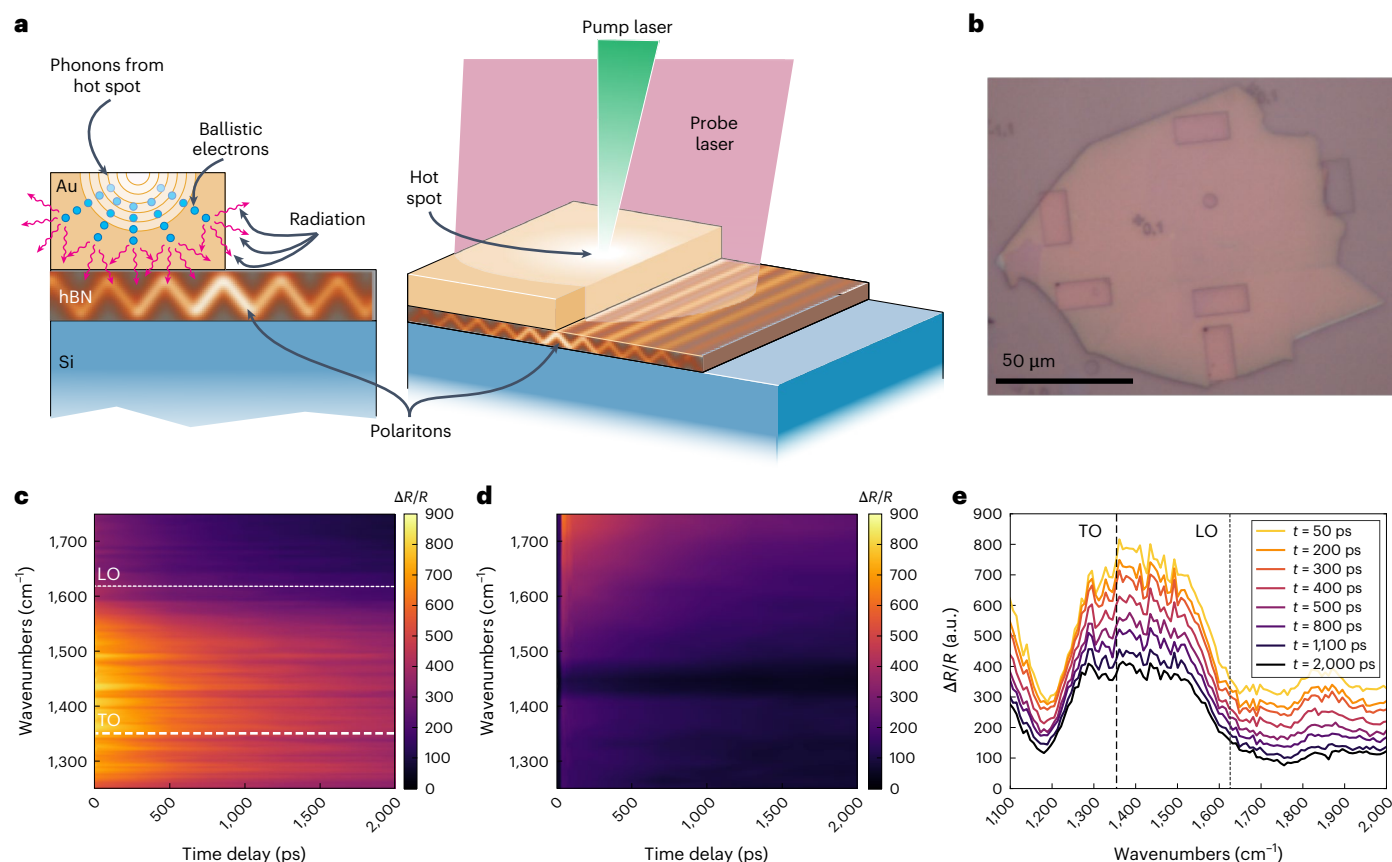


Fig. 1 | Experimental details and spectral-temporal response of HPhP modes in hBN. **a**, Illustration of the proposed mechanism and experimental measurement. A pump pulse (520 nm) heats a gold pad, while a subpicosecond tunable mid-IR probe pulse measures the modulated reflectivity response of the hBN patterned flake. After pulse absorption in the Au, both phonons and ballistic electrons spread from the hot spot in the Au, depicted by the small blue particles and the background waves emanating from the hot spot. Radiation from the hot electrons (red arrows) escapes and couples into the HPhP modes of hBN (pump and probe spot sizes not to scale). **b**, The sample geometry. The reliefs in the image show the position of Au excitation pads used for both s-SNOM characterization (Methods), as well as thermal HPhP launching. **c**, The measured thermorefectance signal of the 116-nm hBN flake as a function of probe energy and pump-probe delay time for an incident pump fluence of 95.5 J m^{-2} . The strong $\Delta R/R$ response within the Reststrahlen band (indicated by the span of the

dotted lines) and near the TO phonon frequency of hBN shows the high thermal activity within the region that can be attributed to ultrafast heating from near-field radiation emitted by the Au pad. **d**, For reference, a similar pump fluence of an uncoated (no Au) hBN flake is provided, noting that in this case, no temporal thermorefectance response is observed within the range of the hBN Reststrahlen band, illustrating the critical role of the Au pad as a thermal transducer in this experiment. The dark band that appears in the middle of the blank hBN contour is attributed to polymethyl methacrylate residue, a photo-resistive polymer in the lithographic patterning process. **e**, Waterfall plots of the data shown in **c** at a variety of pump-probe time delays (80–2,030 ps) following transient Au heating, indicating more clearly the ultrafast optical response surrounding the TO phonon mode and within the hBN Reststrahlen band (indicated by the span of the dotted lines).

on our thermorefectance signal clearly illustrates that the underlying Si substrate is not playing any meaningful role, as even though it will absorb the pump photons, it does not induce a strong transient spectral response, further demonstrated by supplemental spectral measurements on identical Si substrates (Supplementary Fig. 5).

The observation of a strong thermorefectance signal within the Reststrahlen band at picosecond timescales indicates the role that HPhPs play in this thermal dissipation process. As evidence of this, when we tune our probe energy to frequencies above the Reststrahlen band of hBN following the pumping of the adjacent gold pad, we see minimal temporal changes in the probe thermorefectance signal (Fig. 1c,e, dashed vertical lines designating the TO phonon mode and the surrounding active region). However, as the probe energy is tuned to energies within the Reststrahlen band, the thermorefectance signal exhibits large increases in the thermorefectance that is maximized at the earliest times, indicative of large optical phonon temperature changes⁵³ (with an additional peak at the TO phonon energy; Fig. 1e, dark vertical dashed line). This considerable increase in thermorefectance drops at frequencies below the TO phonon, with the broadening

below this band potentially owing to the deeply subwavelength modes that can also be stimulated in hBN due to the exceptionally high refractive index within this spectral range, as previously discussed for Mie resonators in 4H-SiC nanopillars⁵⁴. The hBN dielectric function does not vary with thickness in this spectral region^{55,56}. To support this posit, similar observations were made when we performed measurements on hBN flakes with varying thicknesses ranging between 89 nm and 195 nm, an example of which is presented in Supplementary Fig. 6, and as expected, no size effects are observed.

The sample was constructed such that only ~6% of the probed region is covered with gold (Fig. 1b), effectively diminishing any effect that it might have on the measured thermorefectance. Yet we observe a spectrally local thermal event occurring in the Reststrahlen band of hBN. Our lock-in detection scheme isolates any optical effects of the probe. Further, the polaritonic modes in the hBN cannot be launched directly owing to the lack of a momentum-matching condition from the 520 nm pump. Owing to the long time constant of phonon conduction (thousands of picoseconds) compared with the decay time of our observed modal heating, we posit that the Au-to-hBN interfacial heat

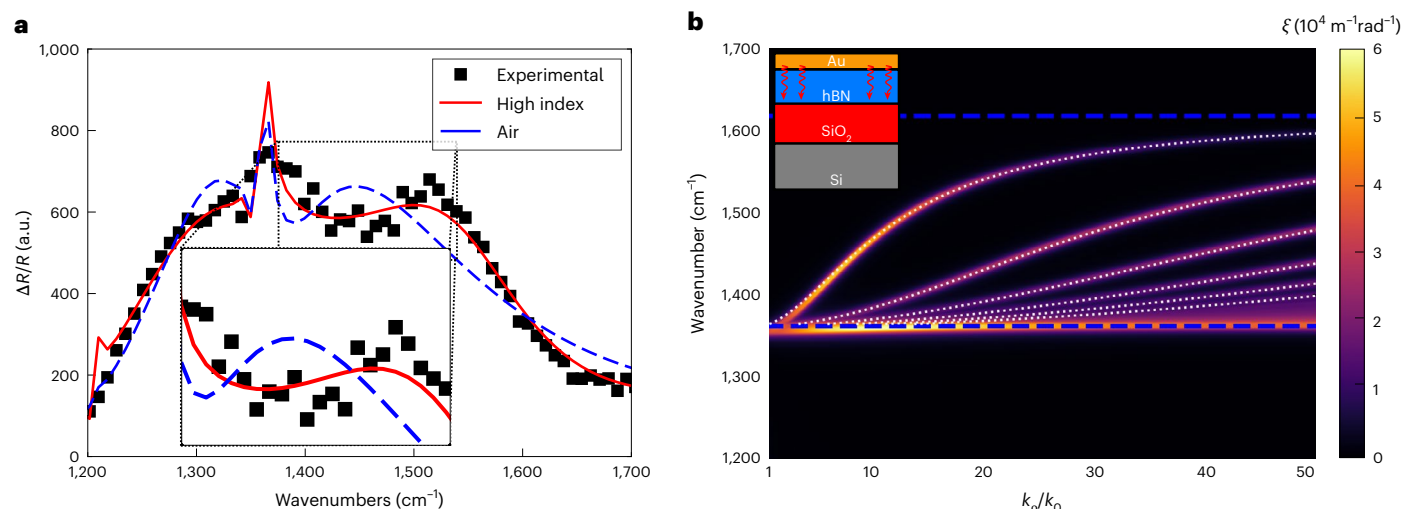


Fig. 2 | Spectral response of hBN after heating from radiating Au pad.

a, The spectral cross sections from the contour of the 116-nm flake (Fig. 1e) fitted with and without a polaritonic coupling layer for a pump–probe delay time of 45 ps. The spectral–temporal range is representative of the entirety of the activity surrounding the TO phonon mode and shows the improvement of the ‘Polaritonic’ model compared with the standard ambient model (‘Air’). The inset plot highlights the advantage of using the high-index layer for momentum matching in the TMM calculation. This ‘high-index layer’ is a better analogue to the near-field radiation from the central gold pad, effectively increasing sensitivity to the TO phonon band and the polaritons therein. **b**, The calculated

spectral heat flux per unit wave vector between Au and hBN layers in contact.

The inset shows a schematic of the simulated stack. The dotted white lines show the dispersion relation of HPhPs in hBN, and the horizontal blue lines show the upper and lower limits of the hBN Reststrahlen band. The fluctuational electrodynamic-derived contour directly shows that the majority of radiative heat flux across the interface is dominated by modes at the same momentum as HPhPs and thus satisfying our proposed launching condition. This plot begins at a normalized wave vector of 1, which means that all representative momenta are considered in the evanescent regime.

transfer mechanism is driven by evanescent pumping of the hyperbolic modes in the hBN flake from the radiating Au pad. This mechanism is mediated by the excited carriers in the Au pad. Owing to the short time-scale of our observed modal heating (tens of picoseconds), we assert that these carriers are the ballistic electrons in the Au that release their heat radiatively at the Au–hBN interface, initiating the ΔT required for radiative transfer.

To further explore the role of HPhPs in the ultrafast interfacial thermal transport between Au and hBN discussed above, we examine the thermoreflectance changes as a function of probe energy measured at short (45 ps; Fig. 2a) pump–probe delay times. We employ the transfer matrix method (TMM⁵⁷, details in the Supplementary Information) to simulate the thermoreflectance spectra in the vicinity of the Reststrahlen band using two models. First, we simulate this differential reflectance spectra by employing a plane wave excitation (‘Air’), which lacks the high-momenta modes sufficient to launch HPhPs in hBN (Fig. 2a, dashed blue line). In contrast, we also perform these TMM calculations using a fictional high-index prism to increase the momentum of optical modes to enable the direct launching of HPhPs (Fig. 2a, red line)⁵⁸. This bending of the light line is effectively a simulation of the reflectivity from an attenuated total reflection module of a Fourier transform infrared system, which has been experimentally shown to launch polaritons^{59–61}. This simulation is therefore an approximation of the reflectivity of a system while there are active polaritons in the system. A full list of fitted parameter perturbations is available in the Supplementary Information. While no prism is employed in the experiments, this is employed as a simple method for simulating the role of the dramatically increased momenta of light, akin to using local dipole coupling to illustrate the role of polaritonic modes within this process. Note that this polaritonic-driven model provides a substantial improvement in the fit as compared with the same model without the momentum-matching conditions (‘Air’), providing further evidence for the role that HPhPs play in this thermal dissipation process. This effect is heavily muted at longer timescales, whereby other thermal dissipation processes, such as

phonon-mediated conduction across the Au–hBN interface begin to dominate (Supplementary Information).

Radiative transport calculation

To determine the exact radiative conditions at the Au–hBN interface explored in Fig. 2b, we explored the distribution of the spectral radiative heat flux over different momenta. Using the framework of the fluctuational electrodynamics⁶², the radiative heat flux between the Au pad and hBN slab can be calculated as

$$q''_{\omega} = \frac{\Theta(\omega, T_{\text{Au}}) - \Theta(\omega, T_{\text{hBN}})}{4\pi^2} \sum_{\gamma=\text{TE, TM}} \left(\int_0^{\pi/a} k_p \xi^{\gamma}(k_p, \omega) dk_p \right), \quad (1)$$

where k_p is the parallel component of the wave vector, Θ is the mean energy of an electromagnetic state, a is the lattice constant of hBN and T_{Au} and T_{hBN} are the temperatures of the Au and hBN layers, respectively. Additionally, ξ^{γ} is the energy transfer function, representing spectral radiative heat flux per unit k_p , between gold and hBN for γ (TE or TM) polarization. Assuming one-dimensional (that is, infinitely long) layered media, the energy transfer function is numerically calculated using scattering matrix method and dyadic green’s functions⁶³. The contour in Fig. 2b shows the energy transfer function between the gold and hBN layers. The dotted white lines in Fig. 2b show the dispersion relation of the HPhPs in hBN, found from the following equation¹¹

$$k_p = \text{Re} \left\{ -\frac{\psi}{d} \left[\tan^{-1} \left(\frac{\epsilon_{\text{Au}}}{\epsilon_{\perp} \psi} \right) + \tan^{-1} \left(\frac{\epsilon_{\text{SiO}_2}}{\epsilon_{\perp} \psi} \right) + \pi l \right] \right\}, \quad (2)$$

where

$$\psi = \frac{\sqrt{\epsilon_{\parallel}}}{i\sqrt{\epsilon_{\perp}}}, \quad (3)$$

where ϵ_{Au} and ϵ_{SiO_2} represent the dielectric function of gold and silica, respectively, ϵ_{\parallel} and ϵ_{\perp} are the parallel and perpendicular dielectric func-

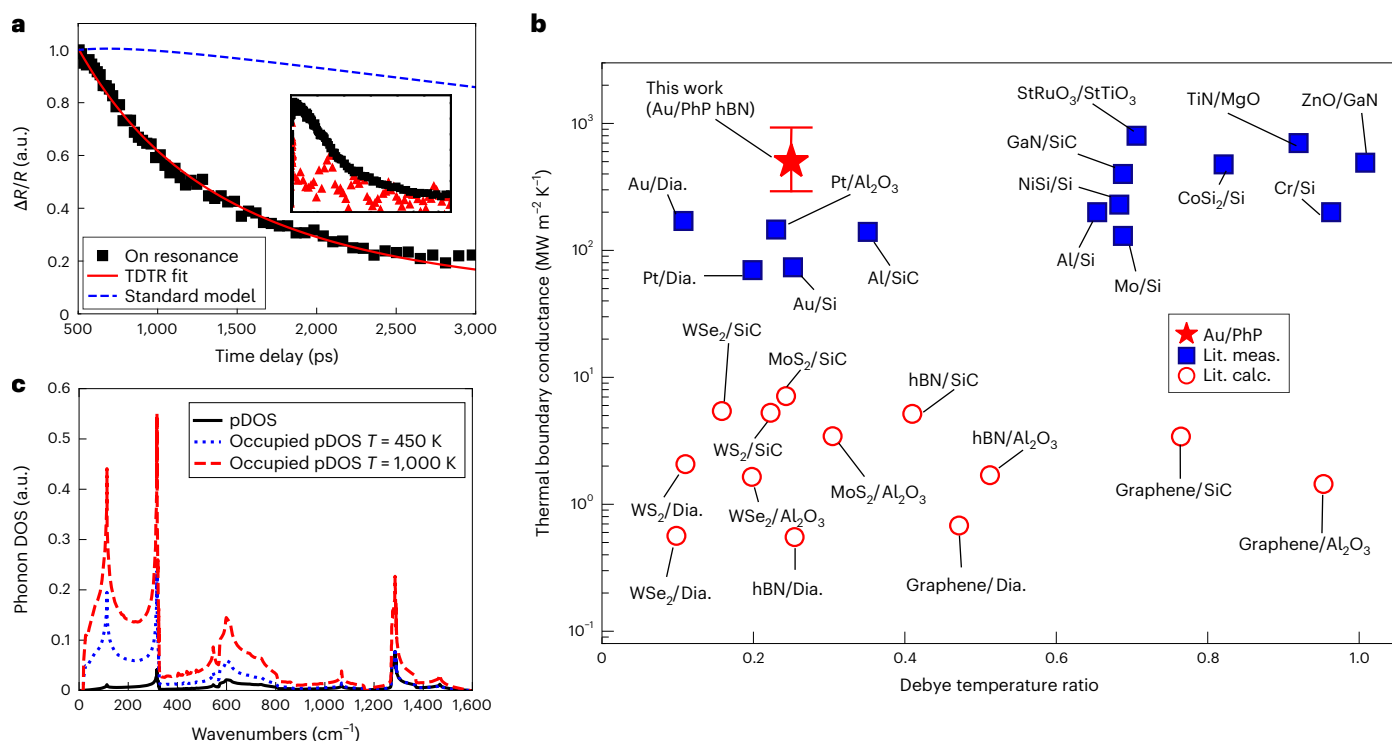


Fig. 3 | Results from thermal analysis of IR thermoreflectance. a, The thermoreflectivity response of hBN as a function of the pump–probe delay time after Au pad heating near the TO resonant frequency (black squares, 7.4 μm) of hBN alongside the analytical model fit to the on-resonance data (solid red line). The best fit for the on-resonance data shown resulted in a HPhP-mediated TBC of $>500 \text{ MW m}^{-2} \text{K}^{-1}$. The standard model (dashed blue line) shows the calculated thermoreflectance signal expected at the surface of the Au pads assuming literature thermal parameters as well as an Au–hBN phonon–phonon TBC of $12.5 \text{ MW m}^{-2} \text{K}^{-1}$ measured with TDTR (see the Supplementary Information for details); the inset shows a comparison of the raw signal magnitude on resonance (black squares, 7.4 μm) with off resonance (red triangles, 6 μm). The inset represents the difference in magnitude and curvature between the off-resonance and on-resonance data past time zero, highlighting the strong response from the hBN when compared with the Si substrate as well as the extended duration that

the hBN remains heated for. **b**, The current state of experimentally measured bulk TBCs across 3D/3D material interfaces (filled blue squares)² as well as predicted 2D/3D interface conductances (open red circles region)⁷⁴ and the best fit Au–hBN HPhP TBC measured in this work with error bars derived from the $\pm 5\%$ contour uncertainty presented in Supplementary Fig. 9, all plotted against a film to substrate ratio of Debye temperatures. **c**, The phonon density of states (pDOS) for hBN was reproduced from a figure in ref. 13 using density functional theory plotted with the occupied density of states at the two temperatures showing the lack of activity in the TO phonon mode 150 K above the ambient temperature, implying that the measurements in this work are due to optical phonon activity measured via IR probing, and not from thermally excited phonon modes from conduction alone. Lit. meas., literature measurements; Lit. calc., literature calculations; Dia., diamond.

tion of hBN, respectively, and l is an integer number corresponding to the order of the HPhP modes. Figure 2b shows that the radiative heat emitted by gold is predominantly received by HPhPs in hBN as the heat flux mostly occurs at wave vectors that precisely match the dispersion of HPhPs. As such, the radiative heat flux at any temperature differential between gold and hBN will be carried predominantly through HPhPs.

Beyond the spectral response, it is also critical to quantitatively analyse the temporal relaxation of the thermoreflectance signals within and outside of the Reststrahlen band to delineate the role that HPhPs play in this process. The stark contrast between the time-dependent thermoreflectance signals under these two distinct conditions are provided as a function of pump–probe delay at a probe energy approximately ‘on resonance’ (Fig. 3a, black squares) with the TO phonon (probe energy of 7.4 μm , 0.17 eV, $1,351 \text{ cm}^{-1}$) compared with the signal with a probe energy ‘off resonance’ (Fig. 3a, pink triangles), which is spectrally separated from the Reststrahlen band of hBN (probe energy of 6 μm , 0.21 eV, $1,667 \text{ cm}^{-1}$), where hBN is nominally transparent to the probe beam (Supplementary Fig. 3). Additionally, at these photon energies, the thermoreflectance changes in Au provide nearly an order of magnitude smaller thermoreflectance signal compared with that measured from the hBN within the Reststrahlen band, thereby precluding any non-negligible transient response from Au in driving the observed response. Thus, as the large bandgap of hBN ($\sim 5.95 \text{ eV}$)

precludes direct absorption of the incident pump energy (2.38 eV), the measured thermoreflectance signal is instead driven by the changes in the temperature of the hBN that are the result of thermal transport from the heated gold across the interface. The dominant signatures at picosecond timescales occur within the Reststrahlen band of hBN, illustrating the strong correlation of these excitations with thermal transport mediated by optical phonons and HPhPs. Further, our control measurement of pumping and probing directly on the hBN in the absence of Au results in a negligible response (Supplementary Fig. 4), clearly indicating that the measured signal (Fig. 3a) is due to a remote heating effect initiated via pump absorption within the Au pad. Thus, the correlation between the ultrafast heating of Au with the dramatic changes in the hBN thermoreflectance within the Reststrahlen band at picosecond timescales clearly illustrates that the mechanism is mediated through the launching of HPhPs via near-field thermal radiation from the heated gold pads. Our results therefore qualitatively suggest that the Au–hBN TBC can be substantially influenced by energy transfer across the Au–hBN interface at ultrafast timescales (subnanosecond) mediated by HPhPs.

Determination of polaritonic conductance rate

The data on resonance with the hBN Reststrahlen band shown in Fig. 3a exhibit an exponential decay with a time constant of $\sim 1,300 \text{ ps}$. After

laser pulse absorption of the gold and the resultant electron–phonon equilibration and thermalization, the majority of the temporal thermal decay is driven by the discharge of energy from the thermalized Au pads into near-field thermal radiation and direct launching of the HPhPs in the hBN. The TBC across the Au–hBN interface from this process can be approximated by $C_v d \tau^{-1} \approx 100 \text{ MW m}^{-2} \text{ K}^{-1}$, where C_v is the heat capacity of the gold, d is the Au film thickness and τ is the time constant of the thermal decay⁶⁴. While this calculation is approximate, it suggests that the heat transfer mechanisms that describe the on-resonance data take place at a rate that is nearly an order of magnitude faster than the phonon–phonon driven TBC across the same Au–hBN ($12 \pm 2 \text{ MW m}^{-2} \text{ K}^{-1}$ on the same hBN sample) measured using time-domain thermoreflectance (TDTR; details the Supplementary Information). To quantify this Au–PhP hBN TBC more rigorously, we solved the analytical solution to the cylindrical heat equation commonly used to fit standard TDTR data⁶⁵ and fit this solution to our data. This solution predicted a TBC of at least $500 \text{ MW m}^{-2} \text{ K}^{-1}$, restricted to a lower bound owing to sensitivities (details in the Supplementary Information). This Au–PhP hBN TBC is roughly one to two orders of magnitude higher than phonon–phonon TBCs measured across a plethora of 3D and 2D material interfaces (Fig. 3b).

It is of note that our model (Fig. 3a) predicts a $\sim 300\times$ increase in effective in-plane polariton conductance in the hBN, consistent with the literature showing enhanced thermal transport in the in-plane direction of hBN owing to polaritonic coupling^{26–28}. These relative increases in local polaritonic conduction can be reasoned on the basis of examining the maximum allowed near-field heat flux, q''_{max} , which is predicted as⁶⁶

$$q''_{\text{max}} = \frac{k_b^2 \left(\frac{\pi}{a}\right)^2}{48\hbar} (T_{\text{emitter}}^2 - T_{\text{absorber}}^2), \quad (4)$$

where the maximum flux allowed in the near field for a Au–hBN interface can lead to a maximum TBC ($G_{\text{max}} = \frac{q''_{\text{max}}}{T_{\text{Au}} - T_{\text{hBN}}}$) of $2.5 \text{ GW m}^{-2} \text{ K}^{-1}$.

Thus, with the coupling of emitted Au energy into hBN hyperbolic modes and non-ideal transfer within this process, the predicted TBC of $500 \text{ MW m}^{-1} \text{ K}^{-1}$ is reasonable. In the same regard, the group velocity of the local phonon modes, which harbour HPhPs, is given by the slope of the dispersion⁶⁷, which is near zero at the zone centre. In contrast, the velocities of the launched hyperbolic modes can be approximated similarly from their dispersion¹¹. From kinetic theory⁶⁸, the thermal conductivity of a system is directly proportional to these velocities, and as the group velocities of hyperbolic modes approach large percentages of the speed of light, the radiative energy flow within these modes will be transferred by the polaritons, thus increasing heat transfer. This enhanced TBC is also supported using a fit to the solution of the one-dimensional heat equation described previously (Supplementary Information)⁶⁹, further supporting that the value for Au–hBN TBC is quantifiably larger than that owing to phonon–phonon conduction alone, and is not a derivative of the assumptions used in our data reduction. We repeat these measurements and calculations on three different Au patterns across two different hBN samples, with a consistent enhancement in Au–hBN thermal conductance observed among all ‘on-resonance’ data.

Measurements of polaritonic launching are often performed directly with the use of a scattering-type scanning near-field microscopy (s-SNOM), which allows for the direct excitation and measurement of polaritonic modes^{12,18–21,36,58}. However, by the nature of measurements in the near field, the system requires careful alignment and interpretation to isolate the effect of the tip launching and nearby reflecting sites. Using far-field optics, our measurement scheme is able to lock-in to the thermal event in the Au pad and probe the thermal trace of the polaritons through changes in reflection of the Brillouin zone centre TO optical modes and neighbouring scattering sites

(Supplementary Information). Thus, our measured signal is isolated temporally from any optical effect caused by the probe and, owing to the high Debye temperature of hBN⁷⁰, the TO phonon would be frozen out at even the maximum lattice temperature predicted by conduction (Fig. 3b). This confluence of factors point directly to the launching of heat carrying thermally excited polaritonic modes.

Our solution to the heat equation predicts a maximum temperature rise in the hBN of approximately 150 K under these experimental conditions. While the absolute value of this increase is certainly prone to uncertainties in assumed input values, it is still orders of magnitude lower than temperatures required to thermally activate a substantial portion of the high frequency TO phonon and HPhP modes. Thus, during the experimental measurements, the optical modes are nearly entirely frozen out from conductive lattice heating alone (Fig. 3c). Thus, this implies that the HPhPs are not excited simply by laser-induced changes in the thermal populations, and instead are stimulated nonthermally through direct launching from near-field radiation emitted from the hot Au pad, further supporting our observations of indirect polaritonic coupling, and resultant energy transfer via HPhP-driven TBC.

Ultrafast heat sink effect

To further confirm this conclusion, we measured the near-IR pump–probe response of the Au surface. Figure 4a illustrates the normalized magnitude of the data taken from a pump probe scan on the surface of the gold in the cases of a silicon substrate and an hBN flake. The Au seems to be dramatically cooler in the case of the hBN substrate at early times, strengthening the evidence for the ultrafast cooling mechanism described above. The models outlined in the insets are similar to those used in the case of the mid-IR probe, where the two temperatures (T_p and T_c) of the Au transducer couple to the temperatures in the substrate. In the case of silicon, when there is no polaritonic coupling in the substrate, only one temperature (T_p) is considered for the substrate, resulting in a two-temperature model (TTM). For a hBN substrate, however, it was found that the early time curvature could not be fit unless a third temperature (T_{HPhP}) to reduce the heat was considered to account for the polaritonic coupling, hence leading to a three-temperature model (3TM). The insets further illustrate the coupling mechanisms for which the model was fitted. Figure 4b shows the raw data in the same scans as in Fig. 4a for a comparison of raw magnitude showing that overall the surface was cooler at all times when comparing the two substrates, indicating the superior heat sink capabilities of hBN in the ultrafast time regime. Figure 4c illustrates the relative sensitivity of the near-IR and mid-IR measurement techniques to the polaritonic interface resistances. We can see that the mid-IR experiment is an order of magnitude more sensitive to the mechanism than the surface of the Au beyond 10 ps, whereas the Au surface dominates sensitivity before 10 ps as it is in this time regime that the heat from the electrons is being sunk to the polaritons.

The above observations coupled with the prior demonstrations of direct launching of propagating phonon polaritons via thermal emission reported by ref. 41 and later by refs. 71,72 indicate a different model whereby HPhPs serve as the dominant thermal transport mechanism at early timescales. Specifically, we propose the following process. First, the ultrafast visible pump is absorbed by the gold pad, which increases its temperature causing it to radiate. Consistent with phonon polariton launching via thermal radiation^{41,72}, the local incoherent dipole moment of the thermal radiation provides the energy matching and momentum matching to directly launch HPhPs within the hBN flake. This in turn stimulates a broad spectrum of HPhP (and TO phonon) modes. Once launched, owing in part to the optical phonon and in part to the light nature of the HPhP quasiparticles, these modes can carry the thermal energy away from the heat source owing to the high heat capacity of the former and the high group velocity (with respect to acoustic phonons) of the latter. A similar mechanism has recently been demonstrated in ref. 73, where under steady state conditions, the thermal conductivity

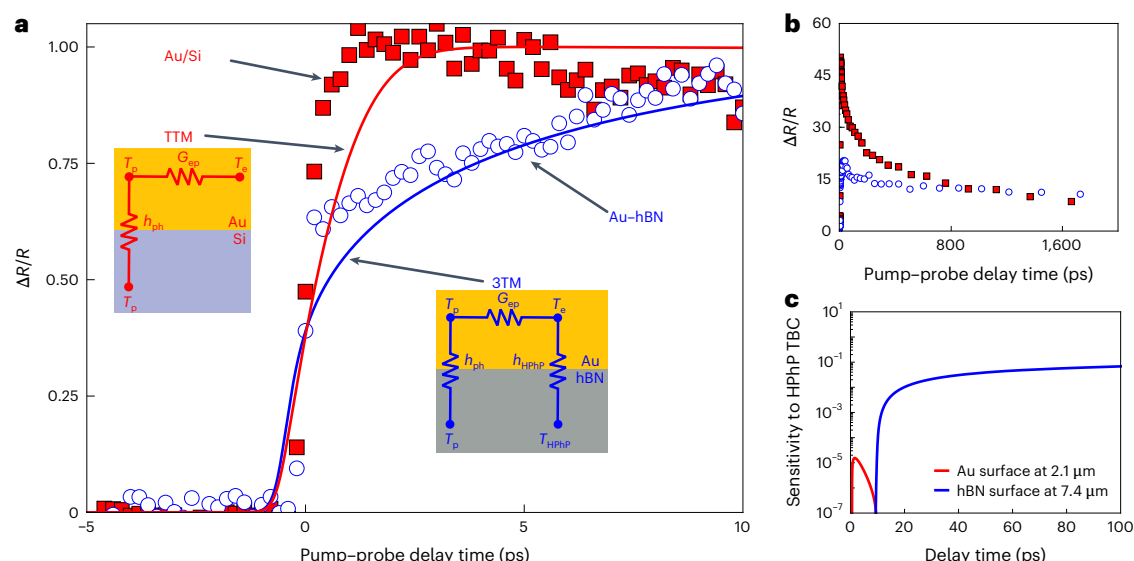


Fig. 4 | Ultrafast pump-probe response of Au on silicon and hBN substrates using a 520-nm pump and 2.1- μm probe. At this probe wavelength, the Drude response in the thermorefectivity of the probe results in sensitivity to the lattice temperature changes in the Au^{53,75}. **a**, The solid squares and open circles show the measured transient lattice temperature changes in Au when on a Si substrate and hBN substrate, respectively. The Au lattice temperature changes on hBN during and after the 520 nm pump heating is suppressed at shorter pump-probe delay times and takes longer to rise and equilibrate when coupling to the excited electrons in the Au as compared to the case when Au is on a Si substrate. This is owing to an additional energy loss pathway of the hot electrons in the Au to the

hBN substrate, the trends of which we capture with a 3TM that accounts for a gold electron to hBN HPhP-optical phonon energy transport pathway (h_{HPhP}), shown as a solid blue line assuming this pathway's TBC is $500 \text{ MW m}^{-2} \text{ K}^{-1}$. Note, these ultrafast Au thermorefectance trends are not captured with a TTM, which shows a much faster lattice temperature rise when this Au electron to substrate TBC is not considered and only electron-phonon coupling in the Au (G_{ep}) is considered, indicated by the red solid line. **b**, Un-normalized thermorefectance signal from the data presented in **a**, where the reduced magnitude in the signal indicates the overall enhanced cooling of the Au surface. **c**, The relative sensitivity of the presented measurements to the HPhP interface coupling.

is enhanced by to surface confined PhPs in silicon carbide. Our work extends these findings to volumetric hyperbolic modes and into the ultrafast regime. This ultrafast mechanism is of critical importance, as while the HPhPs will eventually decay back to conductively heat, the local hBN lattice and, thus, thermalization of the energy will result in uniform heating of the flake. At ultrafast timescales, this provides opportunities for extracting the heat from localized hot spots before catastrophic processes occur (such as device failure). Our results should lay the groundwork for a new generation of photonic sources and an efficient transport mechanism for mode specific heat sinks in high frequency electronics.

Here, we have experimentally established the potential for ultrafast, thermal transport across solid-solid interfaces via the transduction of thermal energy from a transiently heated gold pad into HPhPs supported within hBN. This mechanism provides insight into the role that polaritonic modes can offer in the realm of interfacial heat transfer, overcoming the traditional limitations of phonon-dictated TBC. Specifically, we demonstrate that polaritonic coupling can facilitate the optical modes to move heat across and away from a Au-hBN interface over an order of magnitude faster than acoustic phonon conduction in the same system. These investigations serve as the initial exploration into our understanding of the fundamental guiding principles of such ultrafast transport phenomena. Thus, through further studies of polariton-phonon scattering rates and a quantification of energy tunnelling through different interlayers, we hope to elucidate the effectiveness of this energy transfer, including quantifying the maximum heat flux and capacity. The mechanism demonstrated in this work holds pronounced potential for cooling interconnects via radiative absorption. Subsequent research endeavours can leverage this study as a basis for expanding thermal transport to include transducer cooling, as well as enhancing interfacial flow through more precise nonequilibrium experiments. The impact of this new mechanism has two main features that stand out, namely speed and controllability.

Once the thermal energy is being carried by a polariton, it is travelling at ultrasonic speeds, which means that, for high-power or high-frequency electronic devices that accumulate heat via joule heating, this mechanism can remove heat faster than it is accumulated. This would help next-generation devices to maintain safe operating temperatures, even at higher current densities or near local defect-induced hot spots. The ability to design polaritonic modes through selection of materials and patterning of optical devices also allows for several advancements in novel computers, and thermal management. This new mechanism also serves to employ thermal energy to launch polaritons, meaning that photonic circuits may be able to have a useful nanoscale source for photons. Thermally, these results let us design and optimize new devices 'shielded' from evanescent radiation by polaritonic absorbers.

Online content

Any methods, additional references, Nature Portfolio reporting summaries, source data, extended data, supplementary information, acknowledgements, peer review information; details of author contributions and competing interests; and statements of data and code availability are available at <https://doi.org/10.1038/s41563-025-02154-5>.

References

- Swartz, E. T. & Pohl, R. O. Thermal boundary resistance. *Rev. Mod. Phys.* **61**, 605–688 (1989).
- Giri, A. & Hopkins, P. E. A review of experimental and computational advances in thermal boundary conductance and nanoscale thermal transport across solid interfaces. *Adv. Funct. Mater.* **30**, 1903857 (2020).
- Pop, E. Energy dissipation and transport in nanoscale devices. *Nano Res* **3**, 147–169 (2010).
- Chen, G. Size and interface effects on thermal conductivity of superlattices and periodic thin-film structures. *J. Heat Transf.* **119**, 220–229 (1997).

5. Giri, A. & Hopkins, P. E. Achieving a better heat conductor. *Nat. Mater.* **19**, 482–484 (2020).
6. Barker, A. S. Infrared absorption of localized longitudinal-optical phonons. *Phys. Rev. B* **7**, 2507–2520 (1973).
7. Adachi, S. *Optical Properties of Crystalline and Amorphous Semiconductors* (Springer, 1999); <https://doi.org/10.1007/978-1-4615-5241-3>
8. Poddubny, A., Iorsh, I., Belov, P. & Kivshar, Y. Hyperbolic metamaterials. *Nat. Photonics* **7**, 958–967 (2013).
9. Caldwell, J. D. et al. Sub-diffractive volume-confined polaritons in the natural hyperbolic material hexagonal boron nitride. *Nat. Commun.* **5**, 5221 (2014).
10. Caldwell, J. D. et al. Photonics with hexagonal boron nitride. *Nat. Rev. Mater.* **4**, 552–567 (2019).
11. Dai, S. et al. Tunable phonon polaritons in atomically thin van der Waals crystals of boron nitride. *Science* **343**, 1125–1129 (2014).
12. Giles, A. J. et al. Ultralow-loss polaritons in isotopically pure boron nitride. *Nat. Mater.* **17**, 134–139 (2018).
13. Cuscó, R. et al. Isotopic effects on phonon anharmonicity in layered van der Waals crystals: isotopically pure hexagonal boron nitride. *Phys. Rev. B* **97**, 155435 (2018).
14. Ma, W. et al. In-plane anisotropic and ultra-low-loss polaritons in a natural van der Waals crystal. *Nature* **562**, 557–562 (2018).
15. Zheng, Z. et al. Highly confined and tunable hyperbolic phonon polaritons in van der Waals semiconducting transition metal oxides. *Adv. Mater.* **30**, e1705318 (2018).
16. Taboada-Gutiérrez, J. et al. Broad spectral tuning of ultra-low-loss polaritons in a van der Waals crystal by intercalation. *Nat. Mater.* **19**, 964–968 (2020).
17. Passler, N. C. et al. Hyperbolic shear polaritons in low-symmetry crystals. *Nature* **602**, 595–600 (2022).
18. Hu, G. et al. Real-space nanoimaging of hyperbolic shear polaritons in a monoclinic crystal. *Nat. Nanotechnol.* <https://doi.org/10.1038/s41565-022-01264-4> (2022).
19. Pavlidis, G. et al. Experimental confirmation of long hyperbolic polariton lifetimes in monoisotopic (10B) hexagonal boron nitride at room temperature. *APL Mater.* **9**, 091109 (2021).
20. Ni, G. et al. Long-lived phonon polaritons in hyperbolic materials. *Nano Lett.* **21**, 5767–5773 (2021).
21. Li, P. et al. Hyperbolic phonon-polaritons in boron nitride for near-field optical imaging and focusing. *Nat. Commun.* **6**, 7507 (2015).
22. Dai, S. et al. Subdiffractive focusing and guiding of polaritonic rays in a natural hyperbolic material. *Nat. Commun.* **6**, 6963 (2015).
23. He, M. et al. Ultrahigh-resolution, label-free hyperlens imaging in the mid-IR. *Nano Lett.* **21**, 7921–7928 (2021).
24. Salihoglu, H. et al. Energy transport by radiation in hyperbolic material comparable to conduction. *Adv. Funct. Mater.* **30**, 1905830 (2020).
25. Wu, X. & Fu, C. Near-field radiative heat transfer between uniaxial hyperbolic media: Role of volume and surface phonon polaritons. *J. Quant. Spectrosc. Radiat. Transf.* **258**, 107337 (2021).
26. Tielrooij, K. J. et al. Out-of-plane heat transfer in van der Waals stacks through electron–hyperbolic phonon coupling. *Nat. Nanotechnol.* **13**, 41–46 (2018).
27. Principi, A. et al. Super-Planckian electron cooling in a van der Waals stack. *Phys. Rev. Lett.* **118**, 126804 (2017).
28. Yang, W. et al. A graphene Zener–Klein transistor cooled by a hyperbolic substrate. *Nat. Nanotechnol.* **13**, 47–52 (2018).
29. Wang, H. et al. Ultrafast relaxation dynamics of hot optical phonons in graphene. *Appl. Phys. Lett.* **96**, 081917 (2010).
30. Tokmakoff, A., Sauter, B. & Fayer, M. D. Temperature-dependent vibrational relaxation in polyatomic liquids: picosecond infrared pump-probe experiments. *J. Chem. Phys.* **100**, 9035–9043 (1994).
31. Kapitza, P. L. Heat transfer and superfluidity of helium II. *Phys. Rev.* **60**, 354–355 (1941).
32. Chen, D. Z. A., Narayanaswamy, A. & Chen, G. Surface phonon-polariton mediated thermal conductivity enhancement of amorphous thin films. *Phys. Rev. B Condens.* **72**, 155435 (2005).
33. Thompson, D., Zhu, L., Meyhofer, E. & Reddy, P. Nanoscale radiative thermal switching via multi-body effects. *Nat. Nanotechnol.* **15**, 99–104 (2020).
34. Guddala, S. et al. Topological phonon–polariton funneling in midinfrared metasurfaces. *Science* **374**, 225–227 (2021).
35. Ma, W. et al. Ghost hyperbolic surface polaritons in bulk anisotropic crystals. *Nature* **596**, 362–366 (2021).
36. Caldwell, J. D. et al. Low-loss, infrared and terahertz nanophotonics using surface phonon polaritons. *Nanophotonics* **4**, 44–68 (2015).
37. Foteinopoulou, S., Devarapu, G. C. R., Subramania, G. S., Krishna, S. & Wasserman, D. Phonon-polaritonics: enabling powerful capabilities for infrared photonics. *Nanophotonics* <https://doi.org/10.1515/nanoph-2019-0232> (2019).
38. Yoxall, E. et al. Direct observation of ultraslow hyperbolic polariton propagation with negative phase velocity. *Nat. Photonics* **9**, 674–678 (2015).
39. Caldwell, J. D., Vurgaftman, I. & Tischler, J. G. Mid-infrared nanophotonics: probing hyperbolic polaritons. *Nat. Photonics* **9**, 638–640 (2015).
40. Tervo, E. J., Adewuyi, O. S., Hammonds, J. S. & Cola, B. A. High thermal conductivity in polaritonic SiO₂ nanoparticle beds. *Mater. Horiz.* **3**, 434–441 (2016).
41. Greffet, J.-J. et al. Coherent emission of light by thermal sources. *Nature* **416**, 61–64 (2002).
42. Thompson, D. et al. Hundred-fold enhancement in far-field radiative heat transfer over the blackbody limit. *Nature* **561**, 216–221 (2018).
43. Narayanaswamy, A., Shen, S., Hu, L., Chen, X. & Chen, G. Breakdown of the Planck blackbody radiation law at nanoscale gaps. *Appl. Phys. Mater. Sci. Process.* **96**, 357–362 (2009).
44. Fiorino, A. et al. Giant enhancement in radiative heat transfer in sub-30 nm gaps of plane parallel surfaces. *Nano Lett.* **18**, 3711–3715 (2018).
45. Shen, S., Narayanaswamy, A. & Chen, G. Surface phonon polaritons mediated energy transfer between nanoscale gaps. *Nano Lett.* **9**, 2909–2913 (2009).
46. Sellan, D. P. et al. Phonon transport across a vacuum gap. *Phys. Rev. B Condens.* **85**, 024118 (2012).
47. Song, B. et al. Enhancement of near-field radiative heat transfer using polar dielectric thin films. *Nat. Nanotechnol.* **10**, 253–258 (2015).
48. Warzoha, R. J. et al. Applications and impacts of nanoscale thermal transport in electronics packaging. *J. Electron. Packag.* **143**, 020804 (2021).
49. Aryana, K. et al. Suppressed electronic contribution in thermal conductivity of Ge₂Sb₂Se₄Te. *Nat. Commun.* **12**, 7187 (2021).
50. Aryana, K. et al. Interface controlled thermal resistances of ultra-thin chalcogenide-based phase change memory devices. *Nat. Commun.* **12**, 774 (2021).
51. Fiorino, A. et al. Nanogap near-field thermophotovoltaics. *Nat. Nanotechnol.* **13**, 806–811 (2018).
52. Hohlfeld, J. et al. Electron and lattice dynamics following optical excitation of metals. *Chem. Phys.* **251**, 237–258 (2000).
53. Tomko, J. A., Kumar, S., Sundaraman, R. & Hopkins, P. E. Temperature dependent electron-phonon coupling of Au resolved via lattice dynamics measured with sub-picosecond infrared pulses. *J. Appl. Phys.* **129**, 193104 (2021).
54. Howes, A., Nolen, J. R., Caldwell, J. D. & Valentine, J. Near-unity and narrowband thermal emissivity in balanced dielectric metasurfaces. *Adv. Opt. Mater.* **8**, 1901470 (2020).

55. Kumar, P., Chauhan, Y. S., Agarwal, A. & Bhowmick, S. Thickness and stacking dependent polarizability and dielectric constant of graphene-hexagonal boron nitride composite stacks. *J. Phys. Chem. C* **120**, 17620–17626 (2016).
56. Laturia, A., Van de Put, M. L. & Vandenbergh, W. G. Dielectric properties of hexagonal boron nitride and transition metal dichalcogenides: from monolayer to bulk. *npj 2D Mater. Appl.* **2**, 6 (2018).
57. Passler, N. C. & Paarmann, A. Generalized 4×4 matrix formalism for light propagation in anisotropic stratified media: study of surface phonon polaritons in polar dielectric heterostructures. *J. Opt. Soc. Am. B* **34**, 2128 (2017).
58. Low, T. et al. Polaritons in layered two-dimensional materials. *Nat. Mater.* **16**, 182–194 (2017).
59. Folland, T. G. et al. Probing hyperbolic polaritons using infrared attenuated total reflectance micro-spectroscopy. *MRS Commun.* **8**, 1418–1425 (2018).
60. Dai, S. et al. Efficiency of launching highly confined polaritons by infrared light incident on a hyperbolic material. *Nano Lett.* **17**, 5285–5290 (2017).
61. Bludov, Y. V. & Vasilevskiy, M. I. Resonant Excitation of Confined Excitons in Nanocrystal Quantum Dots Using Surface Plasmon-Polaritons. *J. Phys. Chem. C* **116**, 13738–13744 (2012).
62. Francoeur, M., Mengüç, M. P. & Vaillon, R. Near-field radiative heat transfer enhancement via surface phonon polaritons coupling in thin films. *Appl. Phys. Lett.* **93**, 043109 (2008).
63. Francoeur, M., Pinar Mengüç, M. & Vaillon, R. Solution of near-field thermal radiation in one-dimensional layered media using dyadic Green's functions and the scattering matrix method. *J. Quant. Spectrosc. Radiat. Transf.* **110**, 2002–2018 (2009).
64. Hopkins, P. E., Norris, P. M. & Stevens, R. J. Influence of inelastic scattering at metal-dielectric interfaces. *J. Heat Transf.* **130**, 022401 (2008).
65. Cahill, D. G. Analysis of heat flow in layered structures for time-domain thermoreflectance. *Rev. Sci. Instrum.* **75**, 5119–5122 (2004).
66. Basu, S. & Zhang, Z. M. Maximum energy transfer in near-field thermal radiation at nanometer distances. *J. Appl. Phys.* **105**, 093535 (2009).
67. Gil, B., Cassabo, G., Cusco, R., Fugallo, G. & Artus, L. Boron nitride for excitonics, nano photonics, and quantum technologies. *Nanophotonics* **9**, 3483–3504 (2020).
68. Kittel, C. *Introduction to Solid State Physics* (Wiley, 1996).
69. Jiang, P., Qian, X., Yang, R. & Lindsay, L. Anisotropic thermal transport in bulk hexagonal boron nitride. *Phys. Rev. Mater.* **2**, 064005 (2018).
70. Tohei, T., Kuwabara, A., Oba, F. & Tanaka, I. Debye temperature and stiffness of carbon and boron nitride polymorphs from first principles calculations. *Phys. Rev. B* **73**, 064304 (2006).
71. Lu, G., Tadjer, M., Caldwell, J. D. & Folland, T. G. Multi-frequency coherent emission from superstructure thermal emitters. *Appl. Phys. Lett.* **118**, 141102 (2021).
72. Lu, G. et al. Engineering the spectral and spatial dispersion of thermal emission via polariton-phonon strong coupling. *Nano Lett.* **21**, 1831–1838 (2021).
73. Pan, Z. et al. Remarkable heat conduction mediated by non-equilibrium phonon polaritons. *Nature* **623**, 307–312 (2023).
74. Foss, C. J. & Aksamija, Z. Quantifying thermal boundary conductance of 2D–3D interfaces. *2D Mater.* **6**, 025019 (2019).
75. Hirt, D. et al. Increased thermal conductivity and decreased electron–phonon coupling factor of the aluminum scandium intermetallic phase (Al_3Sc) compared to solid solutions. *Appl. Phys. Lett.* **124**, 202202 (2024).

Publisher's note Springer Nature remains neutral with regard to jurisdictional claims in published maps and institutional affiliations.

Open Access This article is licensed under a Creative Commons Attribution-NonCommercial-NoDerivatives 4.0 International License, which permits any non-commercial use, sharing, distribution and reproduction in any medium or format, as long as you give appropriate credit to the original author(s) and the source, provide a link to the Creative Commons licence, and indicate if you modified the licensed material. You do not have permission under this licence to share adapted material derived from this article or parts of it. The images or other third party material in this article are included in the article's Creative Commons licence, unless indicated otherwise in a credit line to the material. If material is not included in the article's Creative Commons licence and your intended use is not permitted by statutory regulation or exceeds the permitted use, you will need to obtain permission directly from the copyright holder. To view a copy of this licence, visit <http://creativecommons.org/licenses/by-nc-nd/4.0/>.

© The Author(s) 2025

¹Department of Mechanical and Aerospace Engineering, University of Virginia, Charlottesville, VA, USA. ²Interdisciplinary Materials Science Program, Vanderbilt University, Nashville, TN, USA. ³Department of Mechanical Engineering, Vanderbilt University, Nashville, TN, USA. ⁴Tim Taylor Department of Chemical Engineering, Kansas State University, Manhattan, KS, USA. ⁵Department of Materials Science and Engineering, Pennsylvania State University, University Park, PA, USA. ⁶Department of Materials Science and Engineering, University of Virginia, Charlottesville, VA, USA. ⁷Department of Physics, University of Virginia, Charlottesville, VA, USA. ✉ e-mail: josh.caldwell@vanderbilt.edu; phopkins@virginia.edu

Methods

Device preparation

The hBN flakes were prepared from ¹¹B isotopically enriched source crystals by the standard mechanical exfoliation process onto oxygen plasma treated silicon substrates. As reported in ref. 12 and refs. 76,77, the hBN source crystals were produced by precipitation from a molten metal solution using isotopically enriched precursors (nominally 99.4% ¹¹B) provided by a commercial source. To fabricate the samples, the hBN flakes were initially exfoliated onto a bilayer resist transfer wafer where they were imaged optically and via AFM to down select the ideal flakes for these experiments. Transfer of the flakes onto a standard thermal SiO₂ film on a silicon substrate was performed via standard approaches in a home-built 2D material transfer microscope. The gold pads were patterned using electron beam lithography, development, electron beam deposition of a 50-nm-thick gold film, followed by a standard liftoff procedure in *N*-methyl pyrrolidone. The flake sizes were characterized by atomic force microscopy and patterned using electron beam lithography, followed by electron beam deposition of a 50-nm gold film.

IR pump–probe measurements

The IR thermoreflectance measurements were performed using a Spectra-Physics 30-W Spirit laser (369 fs pulses at 1,040 nm with a repetition rate of 500 kHz) to seed a 16-W Spectra-Physics Spirit One OPA for use as a tunable (2–16 μm) probe pulse, as well as an 8-W HIRO SHG box acting as our visible pump. These two laser lines are directed through a standard pump advancing pump–probe system (Supplementary Information). The pump is then focused through a 125 mm focal-length borosilicate lens to a 30-μm spot size. This is then spatially and temporally overlapped with probe pulses that have been focused through a 50 mm CaF₂ to a 100-μm spot. The reflected probe is then spectrally filtered to eliminate pump bleed through and collected by a Vigo Photonics mercury cadmium telluride photodetector. The signal voltage is then passed to a Zurich Instruments UHFLI 600 MHz lock-in amplifier, which amplifies the voltage with via signal boxcar and demodulated by the pump modulation frequency (optically chopped at 301 Hz) into *X* and *Y* signals, which are then recorded alongside the amplified boxcar auxiliary voltage as a change in reflectance and raw reflectance, respectively.

Polariton characterization

Near-field nano-imaging experiments were carried out in a commercial Neaspec s-SNOM based around a tapping-mode atomic force microscope. A metal-coated Si tip of apex radius $R \approx 20$ nm that oscillates at a frequency of $\Omega \approx 280$ kHz and tapping amplitude of about 100 nm was illuminated by a monochromatic quantum cascade laser beam at a free-space incident wavelength $\lambda = 6.9\text{--}6.6$ μm and at an angle 60° off normal to the sample surface, with the incident light being *p*-polarized. As s-SNOM predominantly couples to the *p*-polarized component, the signal detected is dominated by HPhP signals, which can only emerge from *p*-polarized light³⁷. Scattered light launches HPhPs in the device and the tip then rescatters light for detection in the far field⁷⁸. Similar to previous studies of HPhPs using s-SNOM, the presence of the metallic tip will lead to the presence of a tip-launched mode. Background signals were efficiently suppressed by demodulating the detector signal at the third harmonic of the tip oscillation frequency and using pseudo-heterodyne interferometric detection. In s-SNOM images, HPhPs can be observed in two ways: first, polaritons launched by light scattered from the s-SNOM tip propagate radially away from the tip and reflect back from sample boundaries, for example, a flake edge, creating interference fringes with spacing λ_{HPhP} divided by two (as in refs. 11,79,80), which are scattered back to free space by the tip and detected. Alternatively, polaritons can be directly launched from the edge of h11BN flakes and then propagate across the surface and interfere with the incident field at the tip, producing fringes with spacing λ_{HPhP} (refs. 12,59,60). The simulated dispersion

plot is generated using a TMM to determine the reflection coefficients from Fresnel's equations using the reported dielectric function from refs. 12,57 (Supplementary Information).

Data availability

The source data for Figs. 2–4 are provided with this paper. Any other data supporting the findings in this manuscript are available in the Supplementary Information or from the corresponding authors upon reasonable request. Source data are provided with this paper.

References

76. Vuong, T. Q. P. et al. Isotope engineering of van der Waals interactions in hexagonal boron nitride. *Nat. Mater.* **17**, 152–158 (2017).
77. Liu, S. et al. Single crystal growth of millimeter-sized monoisotopic hexagonal boron nitride. *Chem. Mater.* **30**, 6222–6225 (2018).
78. He, M. et al. Guided mid-IR and near-IR Light within a hybrid hyperbolic-material/silicon waveguide heterostructure. *Adv. Mater.* **33**, 2004305 (2021).
79. Fei, Z. et al. Gate-tuning of graphene plasmons revealed by infrared nano-imaging. *Nature* **487**, 82–85 (2012).
80. Chen, J. et al. Optical nano-imaging of gate-tunable graphene plasmons. *Nature* **487**, 77–81 (2012).

Acknowledgements

J.-P.M. acknowledges funding from the National Science Foundation under grant no. NSF-DMR-1904793. K.D.-G., W.H., J.A.T., and D.M.H. were supported by the Army Research Office under grant no. W911NF-21-1-0119. S.Z., T.P. and P.E.H. were supported by the Office of Naval Research under grant no. N00014-23-1-2630. M.H. was supported by the Office of Naval Research under grant no. N00014-22-1-2035. J.D.C. acknowledges support from the Office of Naval Research Multi-University Research Initiative (MURI) on Twist-Optics under grant no. N00014-23-1-2567. J.H.E. and J.L. acknowledge support for hBN crystal growth from the Office of Naval Research, grant no. N00014-20-1-2474.

Author contributions

The project was conceived by J.D.C., P.E.H. and J.-P.M., and all experiments were equally advised by all three authors. The isotopically enriched hBN crystals were grown at Kansas State University by J.L. while under the advisement of J.E. Samples were fabricated by M.H. and J.M. at Vanderbilt University within the Vanderbilt Institute for Nanoscale Science and Engineering. IR spectroscopic and nano-optic probe characterization of hBN flakes was performed by K.D.-G., M.H., M.L. and J.R.M. Far-field tunable mid-IR pump–probe experiments as well as optical and temporal modelling were performed at the University of Virginia ExSITE lab by W.H., D.M.H., J.A.T., S.Z., T.P. and P.E.H.

Competing interests

The authors declare no competing interests.

Additional information

Supplementary information The online version contains supplementary material available at <https://doi.org/10.1038/s41563-025-02154-5>.

Correspondence and requests for materials should be addressed to Joshua D. Caldwell or Patrick E. Hopkins.

Peer review information *Nature Materials* thanks Siyuan Dai and the other, anonymous, reviewer(s) for their contribution to the peer review of this work.

Reprints and permissions information is available at www.nature.com/reprints.